Acoustics of 90 degree sharp bends. Part II: Low-frequency aeroacoustical response

S. Dequand*, S. J. Hulshoff**, Y. Aurégan***, J. Huijnen*, R. ter Riet*, L. J. van Lier*, A. Hirschberg*

*: Technische Universiteit Eindhoven, Postbus 513, 5600 MB Eindhoven, The Netherlands

**: Faculty of Aerospace Engineering, Delft Univ. of Technology, Kluyverweg 1, 2629HS Delft, The Netherlands

***: Laboratoire d'Acoustique de l'Université du Maine, UMR-CNRS 6613, Université du Maine,
    Av. Olivier Messiaen, 72085 Le Mans Cedex 09, France

Summary

The *aeroacoustical* response of 90 degree sharp bends is defined as the response to acoustical perturbations in the presence of a main flow. The *acoustical* response of bends, in the absence of a main flow, has been considered in part I [1]. Experiments are carried out for bends in pipes with circular cross-sections. These 3D-bends have a sharp inner edge and have either a sharp outer corner or a rounded outer wall. The three-dimensional experimental results are compared with results of numerical simulations, based on the Euler equations for two-dimensional inviscid and compressible flows, and with analytical data obtained by means of two-dimensional quasi-steady flow theories. As observed in the absence of a main flow (part I [1]), the two-dimensional numerical simulations provide a good prediction of the aeroacoustical response of bends with a sharp inner edge and a sharp outer corner. For bends with a rounded outer corner, the prediction is less satisfactory. The two-dimensional quasi-steady flow approximation predicts reasonably well the response of bends up to Strouhal numbers of the order of unity. However, quasi-steady flow theories do not predict the irregularities of the response as a function of the flow velocity. These irregularities are expected to be a Strouhal number effect and are observed both in experiments and numerical simulations.

PACS no. 43.20.Mv, 43.20.Ra, 43.20,Fn

1. Introduction

The acoustical response of 90° sharp bends has been presented in part I [1]. We assumed that 2-D and 3-D data correspond to each other for equal dimensionless frequencies f/f_c. The very good agreement observed between experimental, theoretical and numerical data confirms the validity of such an approximation, in the case of a 90° bend with a sharp inner edge and a sharp outer corner. For pipes with circular cross-sections, a surprising result was obtained: experimental data for 3D-bends with a rounded outer corner agreed better with 2-D theory for bends with a sharp outer corner than with 2-D theory for bends with a rounded outer corner. For a stagnant uniform fluid ($\overline{u_1} = 0$), the shape of the outer corner does not seem to have much impact on the acoustical response of the 3-D bend.

The present paper deals with the response of single (isolated) 90° sharp bends to an acoustical perturbation in the presence of a main flow of velocity $\overline{u_1}$. A sharp bend in a pipe has mostly a damping effect for the acoustic field. The flow separation at the bend also affects the aeroacoustic behavior of pipe discontinuities placed downstream of the bend. Examples of such interactions are provided by Ziada [2], [3] for self-sustained oscillations of a closed-side branch system and by Nygård [4] for broad-band noise production by two successive bends. Such effects are not considered here.

The aeroacoustical response of the bends is described in terms of the coefficients of a scattering matrix. The frequency dependence of these coefficients will be given for fixed Mach numbers $M_1 = \overline{u_1}/c_1$ where $\overline{u_1}$ and c_1 represent the main flow velocity and the speed of sound, respectively, in the pipe segment 1 upstream of the bend (Figure 1 in part I [1]). Three-dimensional experimental data obtained from measurements at the LAUM by means of the two-source method (part I [1]) are compared with numerical predictions based on the two-dimensional non linear Euler equations. 2-D and 3-D data are assumed to correspond to each other for equal dimensionless frequency f/f_c (as assumed in part I [1]) and for equal Mach number M_1. Additional experimental data at fixed frequency $f/f_c = 0.043$ are obtained from measurements at TU/e by means of the two-load method. This experimental procedure is described in section 3. The dependence on Mach number M_1 (with $0 \leq M_1 \leq 0.3$) of the reflection and transmission coefficients for the total enthalpy, $R_B^{\pm}$ and $T_B^{\pm}$, respectively, is obtained. Three-dimensional experi-

mental data are compared to results of two-dimensional numerical predictions and quasi-steady flow theories. Note that such a quasi-steady flow approximation appears to be only reasonable for bends with a sharp inner edge. For bends with a rounded inner edge, the deviation of the results obtained by means of the quasi-steady flow theory and the experimental data is larger than the deviation between experimental data for a pipe with a bend and the same length pipe without bend (Dequand [5]).

In section 2, the scattering matrix is defined, the quasi-steady flow theories are briefly explained and the numerical method and its limitations are presented. The experimental procedure is described in section 3. In section 4, numerical predictions are compared to experimental and theoretical data for the 3D-bends with a sharp inner edge and either a sharp or a rounded outer corner (Bends C and D, Figure 1 in part I [1]).

2. Theory

2.1. Scattering matrix

As in the acoustical study (part I [1]), the flow behavior at the bends is described by a scattering matrix $\mathcal{S}_B$. This representation is valid because the frequencies f considered here are low compared to the cut-off frequency f_c, so that only plane waves propagate. In the presence of a main flow, it is more appropriate to introduce the aero-acoustical variable $B_i^{\pm}$ defined as

$$B_i^{\pm} = \frac{p_i^{\pm}}{\rho_i}(1 \pm M_i), \tag{1}$$

where $i = 1, 2$ denotes the pipe segment direction (Figure 1, part I [1]). This variable corresponds to the total enthalpy fluctuations[1] when the entropy fluctuations are neglected. The scattering matrix $\mathcal{S}_B$ relates the different total enthalpy fluctuations:

$$\begin{pmatrix} B_2^+ \\ B_1^- \end{pmatrix} = \underbrace{\begin{pmatrix} T_B^+ & R_B^- \\ R_B^+ & T_B^- \end{pmatrix}}_{\mathcal{S}_B} \begin{pmatrix} B_1^+ \\ B_2^- \end{pmatrix}. \tag{2}$$

When the pipe segment 2 has an anechoic termination ($p_2^- = 0$), the upstream reflection and transmission coefficients for the total enthalpy are:

$$R_B^+ = R_p^+ \left(\frac{1 - M_1}{1 + M_1} \right), \tag{3}$$

$$T_B^+ = T_p^+ \frac{\rho_1}{\rho_2} \left(\frac{1 + M_2}{1 + M_1} \right), \tag{4}$$

where the pressure reflection and transmission coefficients $R_p^{\pm}$ and $T_p^{\pm}$ were introduced in part I [1].

---

[1] Please, note that when the entropy fluctuations are neglected, the total enthalpy may also be called total exergy. However, we use here the term of total enthalpy as used by most authors in the literature (Doak [6], Howe [7]).

When the pipe segment 1 has an anechoic termination ($p_1^+ = 0$), the downstream reflection and transmission coefficients for the total enthalpy are:

$$R_B^- = R_p^- \left(\frac{1 + M_2}{1 - M_2} \right), \tag{5}$$

$$T_B^- = T_p^- \frac{\rho_2}{\rho_1} \left(\frac{1 - M_1}{1 - M_2} \right). \tag{6}$$

2.2. Quasi-steady flow theories

At low Strouhal numbers $S_r = fD/\overline{u_1} \ll 1$ based on the pipe diameter D, we can predict the scattering matrix $\mathcal{S}_B$ by means of quasi-steady flow models as developed by Ronneberger [8] for the pipe expansion and used by Hofmans [9] and Durrieu [10] for the orifice. From their studies, it appears that the aeroacoustical behavior of a diaphragm is already well determined by the jet flow and that the structure of the turbulent mixing region downstream of the jet is not crucial for $S_r < 1$. For low Mach numbers $M_1 \leq 0.1$, it is therefore assumed that an incompressible quasi-steady flow model can be used locally at the bend. For higher Mach numbers, the local flow behavior at the bend is described by a compressible quasi-steady flow model.

The flow is assumed to have a uniform velocity u_1 upstream of the bend. When it reaches the sharp inner edge of the 90° bend, the flow separates and forms a confined jet. The jet reaches a minimum cross-section at which it has a uniform velocity u_j and a cross-section S_j smaller than the pipe cross-section S_p. This is the so-called vena-contracta effect (as observed in the case of a diaphragm [9]). The factor $\Upsilon_j = S_j/S_p$ is called the vena-contracta ratio. Following a turbulent mixing region, the flow becomes again uniform (Figure 1) with a velocity u_2.

2.2.1. Incompressible flow model

In the incompressible flow model, four equations apply:
– the mass conservation equations:

$$S_p u_1 = S_j u_j, \tag{7}$$
$$S_j u_j = S_p u_2, \tag{8}$$

– the Bernoulli equation:

$$p_1 + \frac{1}{2}\rho_0 u_1^2 = p_j + \frac{1}{2}\rho_0 u_j^2, \tag{9}$$

– and the momentum conservation law applied to the turbulent mixing region:

$$S_p p_j + S_j \rho_0 u_j^2 = S_p \left(p_2 + \rho_0 u_2^2 \right). \tag{10}$$

Different assumptions are made:
- only plane waves propagate far away from the discontinuity,
- the source region is compact (small Helmholtz number $S_p k_0^2 = S_p \omega^2/c_0^2 \ll 1$),
- a flow separation occurs at the bend and a jet is formed,
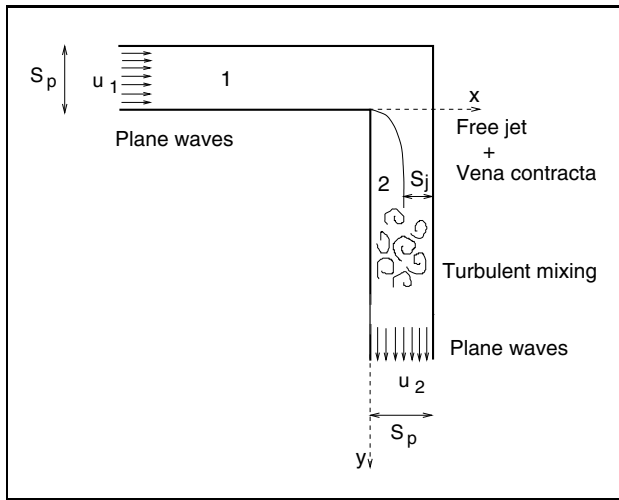- the flow in the jet is incompressible and irrotational,

Figure 1. Quasi-steady behavior of the flow in a sharp bend.

- wall friction and heat transfer are neglected in the turbulent mixing region downstream of the jet and at the walls.

Using this incompressible flow approximation, the scattering matrix $\mathcal{S}$ can be defined as:

$$\mathcal{S} = \begin{pmatrix} T_p^+ & R_p^- \\ R_p^+ & T_p^- \end{pmatrix} = \frac{1}{2 + M_1\beta} \begin{pmatrix} 2 & M_1\beta \\ M_1\beta & 2 \end{pmatrix}, \qquad (11)$$

where $\beta = (S_p/S_j - 1)^2$ takes into account the vena-contracta effect. The incompressible flow assumption is valid for low Mach numbers ($M_1 \leq 0.1$).

2.2.2. Compressible flow model

For higher Mach numbers ($M_1 > 0.1$), the effect of compressibility becomes significant. The four equations of the incompressible flow model (equations 7 to 10) are modified and complemented with the isentropic ideal gas relation (in the upstream region down to the jet) and the energy conservation law. In this model, heat transfer and friction at the walls are neglected. Furthermore, the gas is assumed to have a constant ratio $\gamma = C_p/C_v$ of the specific heats.

$$S_p \rho_1 u_1 = S_j \rho_j u_j, \qquad (12)$$

$$S_j \rho_j u_j = S_p \rho_2 u_2, \qquad (13)$$

$$\frac{1}{2}u_1^2 + \frac{\gamma}{\gamma - 1}\frac{p_1}{\rho_1} = \frac{1}{2}u_j^2 + \frac{\gamma}{\gamma - 1}\frac{p_j}{\rho_j}, \qquad (14)$$

$$S_p p_j + S_j \rho_j u_j^2 = S_p p_2 + S_p \rho_2 u_2^2, \qquad (15)$$

$$\frac{p_1}{p_j} = \left(\frac{\rho_1}{\rho_j}\right)^\gamma, \qquad (16)$$

$$\frac{1}{2}u_1^2 + \frac{\gamma}{\gamma - 1}\frac{p_1}{\rho_1} = \frac{1}{2}u_2^2 + \frac{\gamma}{\gamma - 1}\frac{p_2}{\rho_2}. \qquad (17)$$

In order to take into account the effect of compressibility on the vena-contracta ratio, the empirical formula proposed by Hofmans [9] for an orifice is used:

$$\Upsilon_j = \Upsilon_0 \left(1 + 0.13\frac{\pi + 2}{\pi}M_j^2\right), \qquad (18)$$

where $M_j = \overline{u_j}/c_j$ is the Mach number based on the jet velocity. The determination of the vena-contracta ratio Υ_0 is briefly explained in the next section. The set of equations 12 to 18 is solved numerically, using the incompressible flow approximation as initialization.

2.2.3. Determination of the vena-contracta ratio Υ_0

The vena-contracta ratio Υ_0 can be determined either empirically from the values of the loss-coefficient C_d reported by Blevins [11] and Idelchik [12], or theoretically by means of a potential flow theory as the hodograph method described by Prandtl [13]. The loss coefficient C_d is defined, at low Mach numbers, as the ratio of the pressure difference $\Delta p = p_u - p_d$ (between the pressures upstream and downstream of the bend) and the upstream dynamic pressure:

$$C_d = \frac{p_u - p_d}{\frac{1}{2}\rho\overline{u_1}^2}. \qquad (19)$$

C_d depends on the geometry of the discontinuity and on the Reynolds number $\overline{u_1}D/\nu$ (where D is the pipe diameter and ν is the kinematic viscosity). Following Blevins [11], because the Reynolds numbers are typically of order $O(10^5)$, the values $C_d = 1.2$ for the bend with a sharp outer corner and $C_d = 1.1$ for the bend with a rounded outer wall should be used. These values correspond to the vena-contracta ratio $\Upsilon_0 = 0.48$ and $\Upsilon_0 = 0.488$, respectively. In the limit $M_1 \to 0$, the numerical predictions of steady flow behavior obtained by means of the EIA[2] code converge towards the value $C_d = 1.2$.

The vena contracta ratio Υ_0 of a 2-D bend with a sharp inner edge and a sharp outer corner can also be predicted by means of the potential flow theory (see appendix). The value $\Upsilon_0 = 0.5255$ was found by Huijnen [14]. This corresponds to a loss coefficient $C_d = (S_p/S_j - 1)^2 = 0.8153$. The value $\Upsilon_0 = 0.488$ gave a prediction of the reflection coefficient 20% higher than that predicted with the vena-contracta ratio $\Upsilon_0 = 0.5255$. The theoretical vena-contracta ratio $\Upsilon_0 = 0.5255$ was chosen because it appears to provide a better fit of our experimental data.

2.3. Numerical method

Numerical simulations were performed with the EIA[2] code based on the 2-D Euler equations as described in part I [1]. Acoustical information was obtained by means of the 1-D extraction procedure introduced in part I [1].

The computations were performed in two steps. A steady flow computation was first carried out. This calculation consisted in imposing a constant uniform flow velocity on the upstream boundary of the numerical domain. The inflow velocity magnitude was gradually increased up to the final Mach number $M_1 = \overline{u_1}/c_1$. The time integration was based on a five-stage Runge-Kutta method with a non-time accurate integration. With this method, each cell
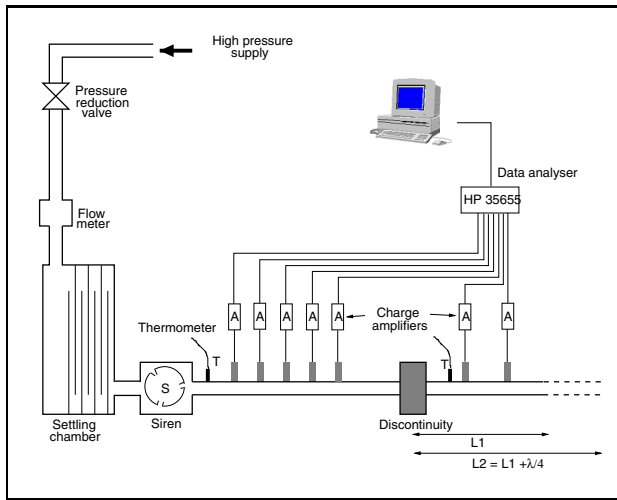
Figure 2. Scheme of the experimental setup used for the two-load method measurements (TU/e - Technical University of Eindhoven). The relative position of the microphones is $x_{12} - x_{11} = -0.1895$ m, $x_{13} - x_{11} = -0.2870$ m, $x_{14} - x_{11} = -0.4843$ m, $x_{15} - x_{11} = -0.5880$ m upstream of the bend, and $x_{22} - x_{21} = 0.3415$ m downstream of the bend. For the bend with a sharp inner edge and a sharp outer corner $x_{11} = -0.1320$ m and $x_{21} = 0.1776$ m. For the bend with a sharp inner edge and with a rounded outer corner $x_{11} = -0.0874$ m and $x_{21} = 0.5598$ m. Note that the reference planes for determining the origin of the phases was chosen at the inner edge of the bend (plane $x = 0$ for $|R_B^+|$ and plane $y = 0$ for $|R_B^-|$) as shown in Figure 1.

is marched at its own stability limit using a different time step. The time needed to get a steady-flow solution is considerably reduced by using this approach compared to a uniform time-step approach. The steady state was obtained when the desired inlet velocity was reached. This solution was then used as initial condition for the unsteady flow computation. This second step is performed by imposing an acoustical perturbation. A right-travelling acoustic wave is applied at the inlet and an anechoic condition is applied at the outlet. The coefficients T_B^+ and R_B^+ can then be determined. The amplitude of the right-travelling acoustic velocity wave was varied from $10^{-3} \times \overline{u_1}$ to $10^{-1} \times \overline{u_1}$. This resulted in a variation of the order of 10^{-3} of the predicted values of the coefficients of the scattering matrix. The coefficients R_B^- and T_B^- can be determined by means of a second calculation in which an upstream-travelling acoustic wave is applied at the outlet while an anechoic condition is applied at the inlet. As in the computations described in part I [1] (in the absence of a main flow), the pressure and the velocity signals were recorded at user-specified numerical probes and had a periodic behavior after typically four periods. The magnitude and the phase of the positive and negative travelling pressure waves p_i^+ and p_i^- were deduced from the recorded pressure and velocity signals using a Fast Fourier Transform of the temporal signals (over six periods).

As explained in section 2.2, the jet formation at the sharp inner edge is followed by a turbulent mixing. Several pipe diameters downstream of the discontinuity, plane

waves should propagate again in a uniform flow. However, due to the absence of effects of viscosity in the model based on the 2-D Euler equations, the 1-D behavior downstream of the bend will never be reached (this is also a problem for the numerical solution which includes dissipative truncation errors, even if a downstream part of ten diameters or more is used as it is needed in experiments to get a uniform flow). This makes the numerical determination of the coefficients T_B^+ and R_B^- of the scattering matrix $\mathcal{S}_B$ difficult and less reliable. In order to overcome this limitation, the plane-wave identification is performed at six diameters D downstream of the bend. A buffer region is added in order to reduce the vorticity at the end of the numerical domain (Figure 6 in part I [1]). This buffer region is placed two diameters downstream of the bend and is made up of blocks with a decreasing number of cells in the direction perpendicular to the pipe axis. This reduces spurious generation of acoustic waves when the vortices leave the calculation domain. For the bend with a sharp inner edge and a rounded outer corner, the coefficients $|T_B^+|$ and $|R_B^-|$ have been determined with an accuracy of 2%. For the bend with a sharp inner edge and a sharp outer corner, the coefficient $|T_B^+|$ has also been determined with an accuracy of 2%. However, the uncertainty in the determination of the downstream reflection coefficient $|R_B^-|$ was of the same order as its own magnitude. Results for $|R_B^-|$ are therefore not presented.

In the bend region, the mesh used for the numerical computations had typically 48 cells both in x and y-directions over a distance $2D$ around the bend.

3. Two-load method

A two-load method was used at TU/e. The setup is described in details by Peters [15], Hofmans [9] and Durrieu [10] and is summarized here.

A scheme of the setup is shown in Figure 2. A high pressure supply system provided dry air at a reservoir pressure between 1 and 15 bar. The valve enabled us to reduce the pressure to the desired level. The volume flux of the air flow was measured by means of a turbine meter. From the measurement of the temperature of the tube wall near the flow meter and near the acoustical measurement section, the temperature of the air flow was deduced by assuming an adiabatic wall recovery temperature with turbulent boundary layer (Shapiro [16]). From the volume flow measurement corrected for pressure and temperature difference, the velocity $\overline{u_1}$ was then deduced. The source used was a siren (rotating valve). The amplitude of the acoustic perturbation generated could be varied. The results shown in the next section were obtained with an amplitude $u_1'/\overline{u_1} = O(10^{-1})$. The settling chamber placed just upstream of the siren contained damping material in order to reduce the effect of acoustic perturbations due to the valves. In the measurement section, the acoustic pressure was measured at different positions by means of piezo-electric pressure transducers (PCB type 116A). The pressure signals were amplified by charge amplifiers
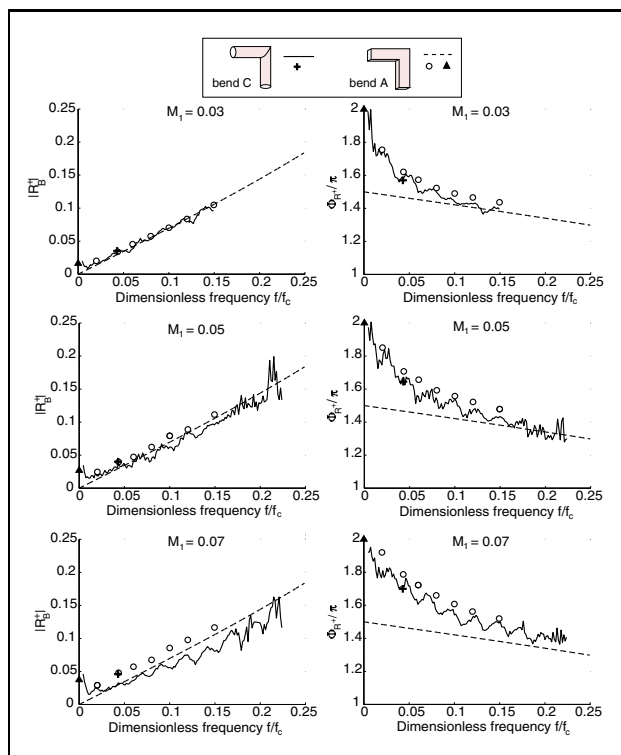
Figure 3. Bend A (and C): Dimensionless frequency dependence of the amplitude $|R_B^+|$ and the phase Φ_{R+}/π of the upstream reflection coefficient for the total enthalpy. Comparison between 3-D experimental results (———) obtained by means of the two-source method and 2-D numerical simulations using EIA (○) for 3 different Mach numbers $M_1 = 0.03$, $M_1 = 0.05$ and $M_1 = 0.07$. The data predicted by the quasi-steady flow theory at $f/f_c = 0$ (▲) and the data obtained at $f/f_c = 0.043$ by means of the two-load method (+) are also plotted. As a reference, the 2-D theory at $M_1 = 0$ (— — —) is shown.
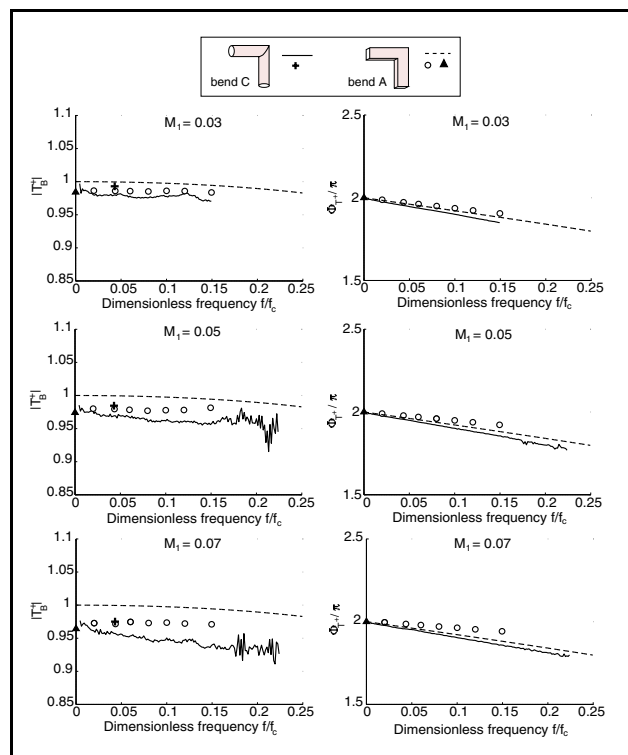

Figure 4. Bend A (and C): Dimensionless frequency dependence of the amplitude $|T_B^+|$ and the phase Φ_{T+}/π of the upstream transmission coefficient for the total enthalpy. Same as in Figure 3. The data obtained at $f = f_c = 0.043$ by means of the two-load method were not available.

(Kistler type 5011). By means of the data-acquisition system (HP3565A and PC), the transfer functions and then the reflection and transmission coefficients were calculated. For convenience, we restricted our measurements to a single frequency $f/f_c = 0.043$. This allowed the choice of optimal microphone positions.

As in the two-source method (introduced in part I [1]), the multiple-microphone method is used to determine the reflection coefficient from the measured transfer functions. For that, five microphones upstream of the discontinuity and two microphones downstream are used. Their positions are given in Figure 2.

The two linearly independent states needed to determine four equations for the coefficients of the scattering matrix $\mathcal{S}_B$, were obtained by measuring with two different acoustic loads. The first measurement was performed with a pipe length $L_1 = 0.6186$ m downstream of the bend. This corresponds roughly to half the wavelength $\lambda/2$ at the frequency ($f = 289$ Hz) used in our experiments, so that the bend is close to a pressure node in this first measurement. The second measurement series was performed with an extra pipe length corresponding to a quarter wavelength ($L_2 = L_1 + \lambda/4$). Such a measurement procedure

requires a rather long time and cannot be accurate when the main flow conditions are not stable. In our setup, the data obtained for the coefficients of the scattering matrix $\mathcal{S}_B$ could be reproduced within 1%.

The frequency dependence of the aeroacoustical response of the bends was measured at the LAUM (Université du Maine, Fr) by means of the two-source method described in part I [1]. In this setup, the Mach number was restricted to $M_1 \leq 0.07$. The data obtained with the two-source method are expected to be more accurate than those obtained by means of the two-load method. The two-load method however enables us to measure at relatively high Mach numbers ($M_1 \leq 0.3$), which could not be reached in the setup at the LAUM.

4. Results

4.1. Frequency dependence

4.1.1. Bends A and C: 90° bend with sharp inner and outer edges

Figures 3 and 4 show the amplitude and the phase of the upstream reflection coefficient ($|R_B^+|$ and Φ_{R+}/π) and of the transmission coefficient ($|T_B^+|$ and Φ_{T+}/π) as a function of the dimensionless frequency f/f_c for the 3-D bend with a sharp inner edge and a sharp outer corner. The results are shown for three different fixed Mach numbers $M_1 = 0.03$, 0.05 and 0.07. The aeroacoustical response
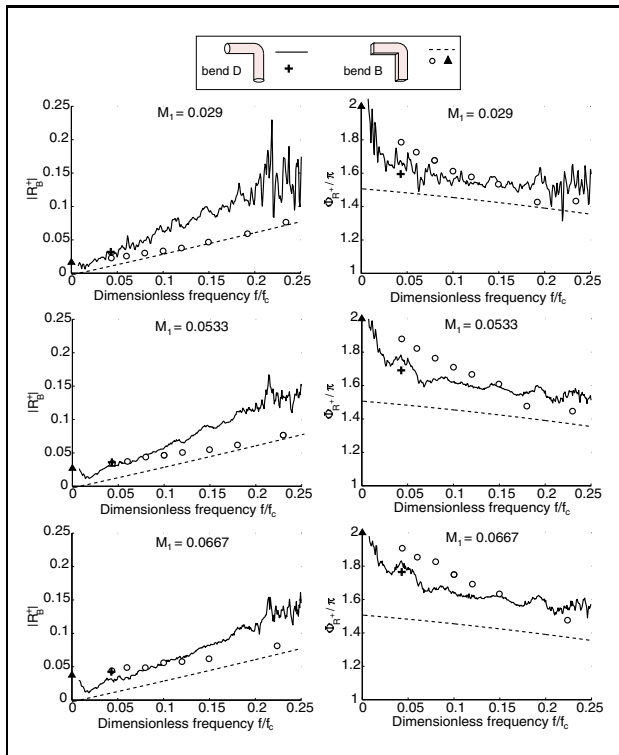
Figure 5. Bend B (and D): Dimensionless frequency dependence of the amplitude $|R_B^+|$ and the phase Φ_{R+}/π of the upstream reflection coefficient for the total enthalpy. Same as in Figure 3.

Figure 6. Bend B (and D): Dimensionless frequency dependence of the amplitude $|T_B^+|$ and the phase Φ_{T+}/π of the upstream transmission coefficient for the total enthalpy. Same as in Figure 3.

of the 3-D bend with circular cross-sections is well predicted by the 2-D numerical simulations. Assuming that 2-D and 3-D data correspond to each other for equal dimensionless frequency f/f_c, we see that at the lowest Mach number $M_1 = 0.03$, the numerical calculations and the experimental results are accurately described by the theory for $M_1 = 0$. Only a significant effect of the main flow in the phase Φ_R^+ of the reflection coefficient R_B^+ is observed. It is also quite interesting to note a difference between the limits $\lim_{f/f_c \to 0} \Phi_R^+ = 1.5\pi$ at $M_1 = 0$ and $\lim_{f/f_c \to 0} \Phi_R^+ = 2\pi$ at $M_1 \neq 0$. The second limit corresponds to the quasi-steady flow theory in which we neglected inertial effects at the bend. The physics of this difference could be similar to that of the difference between the low-frequency limit $S_r \to 0$ at $M_1 = 0$ and the low-frequency limit $He \to 0$ at $M_1 \to 0$ discovered theoretically by Rienstra [17] for the end-correction at an open pipe termination, and confirmed experimentally by Peters [15]. As the Mach number M_1 increases, its influence on the coefficients of the scattering matrix $\mathcal{S}_B$ is observed and is well predicted by the 2-D numerical simulations. When the main flow velocity increases, the deviation between 2-D and 3-D data becomes more important. In the limit of low frequencies, the quasi-steady flow theory is quite accurate.

We also observe that the agreement between the two-source and two-load methods is excellent for the amplitude but much less satisfactory for the phase.
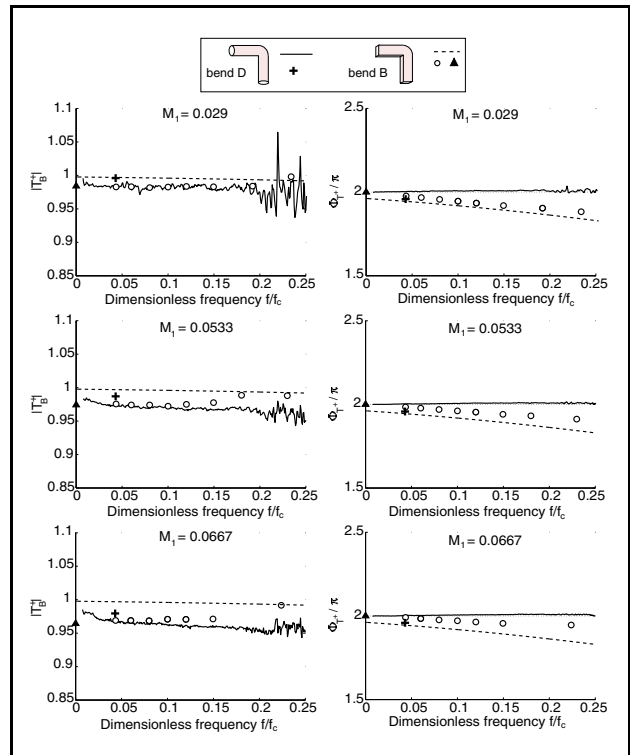
4.1.2. Bends B and D: 90° sharp bend with a rounded outer corner

In figures 5 and 6, the amplitude and the phase of the coefficients of the scattering matrix are presented in terms of the dimensionless frequency f/f_c for three different Mach numbers $M_1 = 0.029, 0.0533$ and 0.0667 for the bend with a sharp inner edge and a rounded outer corner. As observed in the acoustical study presented in part I [1], the deviation between 2-D and 3-D data is much more important for this bend than for the bend with a sharp outer corner. Also for this bend, there is a good agreement between data obtained by means of the two-source and two-load methods.

4.2. Dependence on Mach number

4.2.1. Bends A and C: 90° bend with sharp inner and outer edges

In Figures 7 and 8, the amplitudes $|R_B|$ and $|T_B|$ of respectively the reflection and the transmission coefficients for the total enthalpy are shown as a function of the Mach number $M_1 = \overline{u_1}/c_1$ for a fixed dimensionless frequency $f/f_c = 0.043$. These experimental data are obtained from measurements by means of the two-load method (section 2). The numerical calculations based on the two-dimensional Euler equations predict the amplitudes of the upstream reflection coefficient $|R_B^+|$ and downstream transmission coefficient $|T_B^-|$. In both experimental and numerical results, an irregular behavior of the transmis-
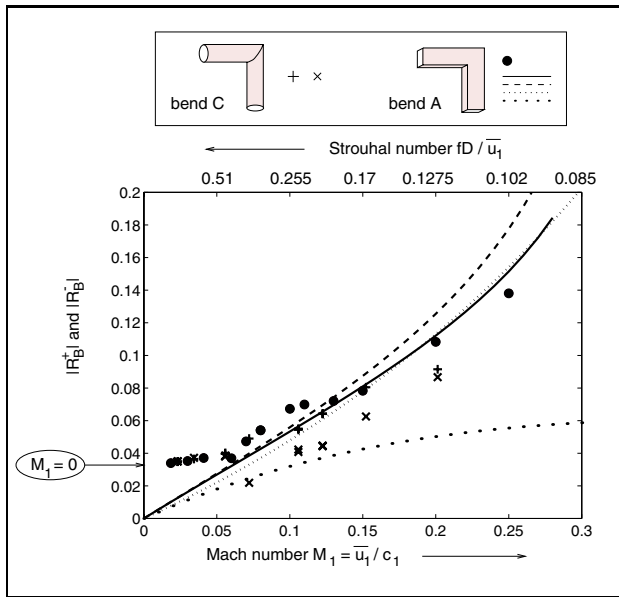
Figure 7. Bend A (and C): Dependence on Mach number of the amplitude of the reflection coefficients $|R_B^+|$ and $|R_B^-|$ for the total enthalpy. The dimensionless frequency is set to $f/f_c = 0.043$. Comparison between 3-D experimental results ($+$ for $|R_B^+|$, $\times$ for $|R_B^-|$) and 2-D numerical simulations ($\bullet$ for $|R_B^+|$). The data are also compared to an incompressible quasi-steady flow theory ($\ldots$ for $|R_B^+|$ and $\ldots$ for $|R_B^-|$) and a quasi-steady compressible flow theory (—— for $|R_B^+|$ and $---$ for $|R_B^-|$).

Figure 8. Bend A (and C): Dependence on Mach number of the amplitude of the transmission coefficients $|T_B^+|$ and $|T_B^-|$ for the total enthalpy. The dimensionless frequency is set to $f/f_c = 0.043$. Comparison between 3-D experimental results ($+$ for $|T_B^+|$, $\times$ for $|T_B^-|$) and 2-D numerical simulations ($\bullet$ for $|T_B^+|$, $\square$ for $|T_B^-|$). The data are also compared to an incompressible quasi-steady flow theory ($\ldots$ for $|T_B^+|$ and $\ldots$ for $|T_B^-|$) and a quasi-steady compressible flow theory (—— for $|T_B^+|$ and $---$ for $|T_B^-|$).

sion coefficient as a function of M_1 is observed around a Strouhal number $S_r = fD/\overline{u_1}$ of 0.2 (Figure 8). The amplitude of the upstream transmission coefficient $|T_B^+|$ is well predicted for low Mach numbers ($M_1 \leq 0.15$). For higher Mach numbers, the upstream transmission coefficient $|T_B^+|$ deviates from the experimental data. This could be due to the difficulties encountered for the plane-wave identification downstream of the discontinuity. These data could only be determined within an accuracy of 2%. The downstream reflection coefficient $|R_B^-|$ is not shown in Figure 7 because the data obtained were not reliable. An alternative extraction method based on an integral method might provide better results (part I [1]). This should be a subject of further research.

Figures 7 and 8 show also the prediction of the quasi-steady incompressible and compressible flow theories for a vena-contracta factor $\Upsilon_0 = 0.5255$. Up to Strouhal numbers of the order of unity (that is for Mach numbers $M_1 \geq 0.07$), the amplitude of the scattering matrix coefficients are reasonably well predicted by the quasi-steady compressible flow theory. For Strouhal numbers of order unity or higher, the experimental reflection coefficient approaches the limit of zero Mach number (part I [1]). It deviates strongly from the quasi-steady flow limit.

The irregularities mentioned above around $S_r = 0.2$ and corresponding to $M_1 = 0.1$, which are observed in experiments and numerical simulations as a function of M_1 (Figure 8), are not predicted by a quasi-steady flow theory. This is expected to be a Strouhal number dependence like the whistling of a diffuser (van Lier [18]) or a grazing
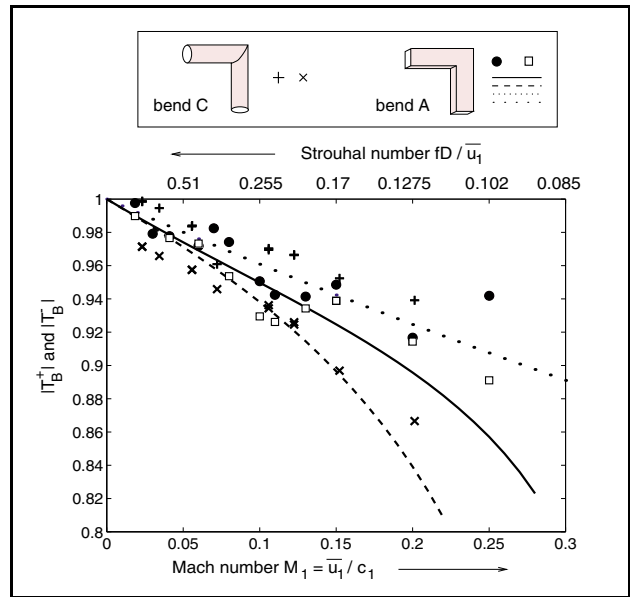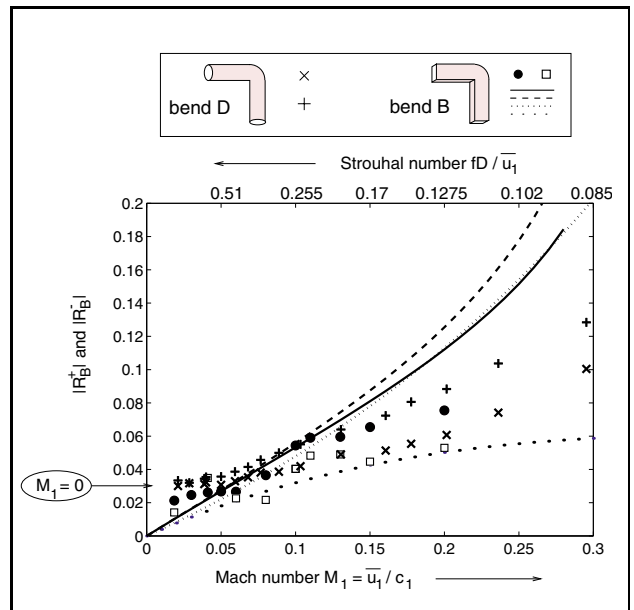

Figure 9. Bend B (and D): Dependence on Mach number of the amplitude of the reflection coefficients $|R_B^+|$ and $|R_B^-|$ for the total enthalpy. Same as in Figure 7.

flow along a Helmholtz resonator (Dequand [19]). Similar particularities have also been observed around $S_r = 0.2$ by Nygård [4] in the broad-band noise produced by a bend with a sharp inner edge and a sharp outer corner. Around $S_r = 0.2$, the broad-band noise of such a bend is 8 dB
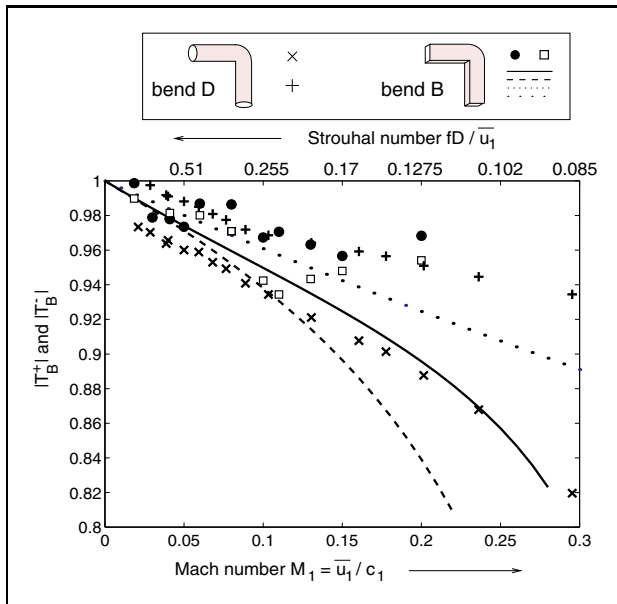
Figure 10. Bend B (and D): Dependence on Mach number of the amplitude of the transmission coefficients $|T_B^+|$ and $|T_B^-|$ for the total enthalpy. Same as in Figure 8.

higher than that of a bend with a rounded outer corner. For bends with a rounded outer corner, the irregularities disappear both in our scattering matrix coefficients and in Nygård's [4] noise measurements. At low Mach number ($M_1 \leq 0.1$), the quasi-steady flow theories give a good prediction of the transmission coefficients $|T_B^+|$ and $|T_B^-|$.

4.2.2. Bends B and D: 90° sharp bend with a rounded outer corner

Results of quasi-steady flow theories have been also compared to 3-D experimental and 2-D numerical data obtained for the 90° sharp bend with a rounded outer corner. The results are shown in figures 9 and 10 in terms of the Mach number. The remarks made in the previous section for the transmission coefficients (Figure 10) apply also here. As observed in part I [1], the numerical prediction of the reflection coefficients (Figure 9) is not as good as in the case of the bend with sharp inner and outer edges. This is expected to be an effect of the comparison between 2-D and 3-D data. The accuracy of the numerical data was around 2%. Note furthermore that the quasi-steady flow theory does not take into account the effect of the geometry of the outer corner. The same value Υ_0 is used in both cases.

5. Conclusions

The aeroacoustic response of 90 degree bends with a sharp inner edge has been studied. Bends with either a sharp or rounded outer corner are considered. In the presence of a main flow ($\overline{u_1} \neq 0$), measurements have been carried out by means of a two-source method and of a two-load method. The first method is best suited to study the response of the bends as a function of the dimensionless frequency f/f_c ($f/f_c \leq 0.15$) for relatively low fixed

Mach numbers ($M_1 \leq 0.07$), while the second method enables a study of the dependence of the response with the Mach number ($0 \leq M_1 \leq 0.3$) for a fixed frequency ($f/f_c = 0.043$). The measurements were performed for pipes with circular cross-sections. These 3-D experimental results are compared to numerical predictions based on the Euler equations for 2-D inviscid and compressible flow and results from 2-D quasi-steady flow theories by assuming that 2-D and 3-D data correspond to each other for equal dimensionless frequencies f/f_c and equal Mach numbers M_1. As observed in the absence of a main flow (part I [1]), this assumption appears to give better results in the case of a bend with a sharp outer corner than in the case of a bend with a rounded outer corner. The main effect of the main flow at low Mach numbers ($M_1 \leq 0.07$) appears to be a drastic change in the behavior of the phase Φ_R^+ of the reflection coefficient R_B^+. A parallel can be drawn between this behavior and the behavior of open pipe terminations in the low-frequency limit where we distinguish the case $S_r \to 0$ at $M_1 \neq 0$ and $He \to 0$ at $S_r \neq 0$.

Up to Strouhal numbers of the order of unity, the amplitude of the scattering matrix coefficients are well predicted by the quasi-steady compressible flow theory. For higher Strouhal numbers, the amplitude of the reflection coefficient approaches the limit of zero Mach number. Quasi-steady flow theories do not predict irregularities of the scattering matrix coefficients. These irregularities are observed both in experiments and numerical simulations and are expected to be a Strouhal number effect. These irregularities around $S_r = 0.2$ are quite pronounced for the bend with a sharp inner edge and a sharp outer corner. Nygård [4] observed in that case a strong enhancement of turbulent sound production compared to the case of the bend with a rounded outer corner.

In the presence of a main flow, numerical predictions of the upstream transmission coefficient T_B^+ and the downstream coefficients R_B^- and T_B^- become difficult due to the non-uniform jet flow which appears after the flow separation at the sharp inner edge of the bends. This makes the extraction of the far-field acoustic response of the bends less accurate while giving the motivation for the use of 1-D extraction regions described in the part I [1]. Further research should be carried out to improve the method of extraction of acoustical data in turbulent flow regions.

Appendix – Hodograph method

The vena-contracta factor introduced in section 2.2 can be determined by means of the hodograph method. The steps of this method are detailed by Prandtl [13] and are briefly described in this appendix. The hodograph method is used to calculate the vena contracta factor of a bend with a sharp inner edge and a sharp outer corner.

The hodograph method is a particular kind of conformal transformation. The principle is to transform the real (x, y)-plane (or z-plane) into the velocity (u, v)-plane (or w-plane). If an analytical expression of the complex po-

tential F in the w-plane is determined, then a relationship between z and w can be obtained by using potential theory.

The complex function $F(z)$ can always be split in a real and an imaginary part:

$$F(z) = F(x + \mathrm{i}y) = \Phi(x,y) + \mathrm{i}\Psi(x,y), \qquad (A1)$$

where Φ and Ψ are the potential and the stream functions, respectively.

Assuming the function $F(z)$ to be analytical, we use the Cauchy-Rieman condition to find:

$$\begin{cases} \dfrac{\partial \Phi}{\partial x} = \dfrac{\partial \Psi}{\partial y}, \\[2mm] \dfrac{\partial \Phi}{\partial y} = -\dfrac{\partial \Psi}{\partial x}. \end{cases} \qquad (A2)$$

As we assume a potential flow, the velocity field can be expressed in terms of the potential function Φ:

$$u = \partial\Phi/\partial x, \qquad (A3)$$
$$v = \partial\Phi/\partial y. \qquad (A4)$$

The total differential dF of the complex function $F(x,y)$ is:

$$\begin{aligned} \mathrm{d}F(z) &= \frac{\partial F}{\partial x}\mathrm{d}x + \frac{\partial F}{\partial y}\mathrm{d}y, \\ &= \left(\frac{\partial\Phi}{\partial x} + \mathrm{i}\frac{\partial\Psi}{\partial x}\right)\mathrm{d}x + \left(\frac{\partial\Phi}{\partial y} + \mathrm{i}\frac{\partial\Psi}{\partial y}\right)\mathrm{d}y, \\ &= (u - \mathrm{i}v)(\mathrm{d}x + \mathrm{i}\mathrm{d}y), \\ &= \bar{w}\mathrm{d}z. \end{aligned} \qquad (A5)$$

This can be written in integral form as:

$$z = \int \frac{\mathrm{d}F(z(\bar{w}))}{\bar{w}} + \text{constant}, \qquad (A6)$$

$$= \int \frac{1}{\bar{w}}\frac{\mathrm{d}\mathcal{F}(\bar{w})}{\mathrm{d}\bar{w}}d\bar{w} + \text{constant}. \qquad (A7)$$

Figure A1 gives a scheme of the streamlines in a sharp bend. Upstream of the bend (point A), the fluid is assumed to flow in the x-direction towards the bend with a uniform velocity $w_A = (a, 0)$. Note that the particular choice of the (x, y) reference frame is made in order to simplify the application of the hodograph method to the bend. At the sharp inner edge of the bend (point C), the flow separates and forms a jet. Downstream of the bend (point B), the flow becomes again uniform with a velocity $w_B = (0, -b)$ and a cross-section S_j smaller than the pipe cross-section S_p, due to the vena-contracta effect. As the pressure along the shear layer bounding the free jet has to be equal to that of the surrounding stagnant fluid, the velocity at point C is $w_C = (b, 0)$ (from Bernoulli's equation). The point D is a stagnation point at which the velocity is zero: $w_D = (0, 0)$.
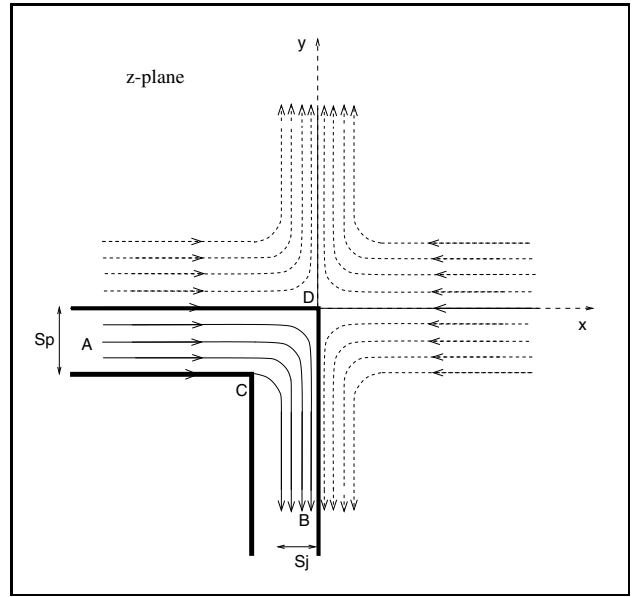

Figure A1. Streamlines in a bend with a sharp inner edge and a sharp outer corner: physical plane (z-plane). The dashed lines correspond to the images.
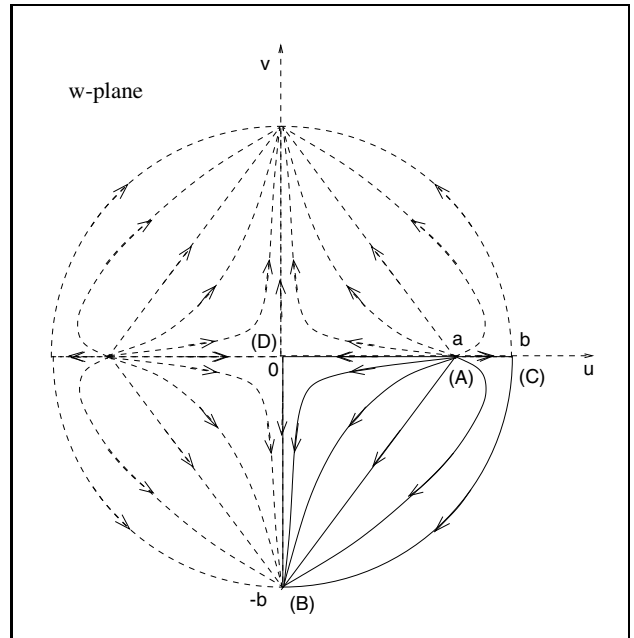

Figure A2. Streamlines in a bend with a sharp inner edge and a sharp outer corner: transformed plane (w-plane) by means of the hodograph method. The dashed lines correspond to the images.

By writing the mass conservation, the vena-contracta factor Υ_0 can be expressed in terms of the velocity values a and b:

$$\Upsilon_0 = \frac{S_j}{S_p} = \frac{a}{b}. \qquad (A8)$$

From the streamlines in the (physical) z-plane shown in figure A1, we can deduce the streamlines in the (hodograph) w-plane (figure A2).

All the streamlines start from point A and go to point B, passing through points C or D. The points A and B are therefore considered as a source and a sink, respectively, and the complex potential $\mathcal{F}_1$ due to their presence would be, in free space:

$$\mathcal{F}_1(w) = \frac{Q_V}{2\pi} \ln(w - a) - \frac{Q_V}{2\pi} \ln(w + ib), \quad (A9)$$

where Q_V is the volume flow.

By adding the effect of mirror images in the $(u = 0)$ and $(v = 0)$-axis, respectively, the complex potential becomes:

$$\mathcal{F}_2(w) = \frac{Q_V}{\pi} \Big[\ln(w - a) + \ln(w + a)$$
$$- \ln(w + ib) - \ln(w - ib) \Big]. \quad (A10)$$

Finally, the presence of the jet is taken into account by using the circle theorem [20]. As the velocity at point C is equal to the velocity at point B, the streamline is a circle of radius $R = b$ and the complex potential becomes:

$$\mathcal{F}(w) = \frac{Q_V}{\pi} \Big[\ln(w^2 - a^2) - \ln(w^2 + b^2)$$
$$+ \ln\left(w^2 - b^4/a^2\right) - \ln\left(w^2 + b^2\right) \Big]. (A11)$$

We find then:

$$\frac{1}{\bar{w}} \frac{d\mathcal{F}(\bar{w})}{d\bar{w}} = \frac{2Q_V}{\pi} \left(\frac{1}{\bar{w}^2 - a^2} \right.$$
$$\left. - \frac{2}{\bar{w}^2 + b^2} + \frac{1}{\bar{w}^2 - b^4/a^2} \right). \quad (A12)$$

By applying equation A7, this yields:

$$z = \frac{Q_V}{\pi a} \left[\ln\left(\frac{\bar{w} - a}{\bar{w} + a} \right) - 4\frac{a}{b} \arctan\left(\frac{\bar{w}}{b} \right) \right.$$
$$\left. + \left(\frac{a}{b} \right)^2 \ln\left(\frac{a\bar{w} - b^2}{a\bar{w} + b^2} \right) \right] + z_0, \quad (A13)$$

where z_0 is the constant of integration.

Equation A13 is now applied to points C and D:

$$z_C = -S_p(1 + i) \qquad (A14)$$
$$= z_0 + \frac{Q_V}{a} \left[\frac{1 + \Upsilon_0^2}{\pi} \ln\left(\frac{1 - \Upsilon_0}{1 + \Upsilon_0} \right) - \Upsilon_0 + i\Upsilon_0^2 \right],$$
$$z_D = 0 = \frac{Q_V}{a} \left(\frac{1 + \Upsilon_0^2}{\pi} \right) \ln(-1) + z_0, \qquad (A15)$$

where $\ln(-1) \equiv i\pi$.

The constant z_0 can be deduced from equation A15:

$$z_0 = -\frac{iQ_V}{a} \left(1 + \Upsilon_0^2 \right). \qquad (A16)$$

Then, equation A14 yields:

$$\varphi = \ln\left(\frac{1 - \Upsilon_0}{1 + \Upsilon_0} \right) \left(1 + \Upsilon_0^2 \right) - \pi\Upsilon_0 + \pi = 0. \qquad (A17)$$

By using Newton's method initialized with the experimental value $\Upsilon_{j0} = 0.48$ found by Blevins [11], we can calculate the vena-contracta factor:

$$\Upsilon_0 = \Upsilon_{j0} - \frac{\varphi(\Upsilon_{j0})}{(d\varphi/d\Upsilon_0)_{\Upsilon_{j0}}} = 0.5255. \qquad (A18)$$

References

[1] S. Dequand, S. J. Hulshoff, Y. Aurégan, J. Huijnen, L. J. van Lier, R. ter Riet, A. Hirschberg: Acoustics of 90 Degree Sharp Bends. Part I: Low-Frequency Acoustical Response. submitted to Acta Acustica.

[2] S. Ziada, E. T. Buhlman: Self-excited Resonances of Two Side Branches in Close Proximity. J. Fluids. Struct. **6** (1992) 583–601.

[3] S. Ziada: Flow Excited Resonances of Piping Systems Containing Side-Branches: Excitation, Counter Measures and Design Guidelines. Seminar on Acoustic Pulsations in Rotating Machinery, Toronto, Canada, 1993.

[4] S. Nygård: Low Frequency Sound in Duct Systems. Tech. Rept. The Marcus Wallenberg Laboratory for Sound and Vibration Research, Royal Institute of Technology, Sweden (ISSN 1103-470X, ISRN KTH/FKT/L 00/57), 2001.

[5] S. Dequand, L. van Lier, A. Hirschberg, J. Huijnen: Aeroacoustic Response of Diffusers and Bends: Comparison of Experiments with Quasi-Stationary Incompressible Models. J. Fluid Struc. **16 (7)** (2002).

[6] P. E. Doak: Fluctuating Total Enthalpy as a Generalized Acoustic Field. Acoustical Physics **44** (1998) 677–685.

[7] M. S. Howe: Acoustics of fluid-structure interactions. Cambridge University Press, 1998.

[8] D. Ronneberger: Experimentelle Untersuchungen zum akustischen Reflektionfaktor von unstetigen Querschnittsänderungen in einem luftdurchströmten Rohr. Acustica **19** (1967) 222–235.

[9] G. C. J. Hofmans, R. J. J. Boot, P. P. J. M. Durrieu, Y. Aurégan, A. Hirschberg: Aeracoustic Response of a Slit-Shaped Diaphragm in a Pipe at Low Helmholtz Number. Part 1: Quasi-Steady Results. J. Sound Vib. **244 (1)** (2001) 35–56.

[10] P. Durrieu, G. Hofmans, G. Ajello, R. Boot, Y. Aurégan, A. Hirschberg, M. Peters: Quasi-Steady Aero-Acoustic Response of Orifices. J. Acoust. Soc. Am. **110** (2001) 1859–1872.

[11] R. D. Blevins: Applied fluid dynamics handbook. Van Nostrand Reinhold Company Inc., New York, 1984.

[12] I. E. Idelchik: Handbook of Hydraulic Resistance: Coefficients of Local Resistance and of Friction. Israel program for scientific translations, Jerusalem, 1966.

[13] L. Prandtl, O. G. Tietjens: Fundamentals of hydro- and aeromechanics. Dover Editions, 1934.

[14] J. H. Huijnen: Aero-Acoustics of a Bend: Quasi-Stationary Models. Tech. Rept. Technische Universiteit Eindhoven, R-1476-A, december 2001.

[15] M. C. A. M. Peters, A. Hirschberg, A. J. Reijnen, A. P. J. Wijnands: Damping and Reflection Coefficient Measurements for an Pipe at Low Mach and Low Helmholtz Numbers. J. Fluid Mech. **256** (1993) 499–534.

[16] A. H. Shapiro: The Dynamics and Thermodynamics of Compressible Fluid Flow, Volume 1. Ronald Press, New York, 1953.

[17] S. W. Rienstra: A Small Strouhal Analysis for Acoustic Wave-jet Flow-pipe Interaction. J. Sound Vib. **86** (1983) 539–556.

[18] L. van Lier, S. Dequand, A. Hirschberg, J. Gorter: Aeroacoustics of Diffusers: an Experimental Study of Typical Industrial Diffusers at Reynolds Numbers of $O(10^5)$. J. Acoust. Soc. Am. **109 (1)** (2001) 108–115.

[19] S. Dequand: Duct Aeroacoustics: from Technological Applications to the Flute. Dissertation. Technische Universiteit Eindhoven (Nl) and Université du Mans (Fr), 2001.

[20] L. M. Milne-Thomson: Theoretical hydrodynamics. 5th ed. London. Mac Millan, 1968.